



HAL
open science

Whispering gallery modes for 3D strain measurement

Yann Lecieux, Dominique Leduc, Corentin Guigot, Marc François, Cyril Lupi

► **To cite this version:**

Yann Lecieux, Dominique Leduc, Corentin Guigot, Marc François, Cyril Lupi. Whispering gallery modes for 3D strain measurement. *Optics and Laser Technology*, 2022, 149, pp.107862. 10.1016/j.optlastec.2022.107862 . hal-04731088

HAL Id: hal-04731088

<https://hal.science/hal-04731088v1>

Submitted on 10 Oct 2024

HAL is a multi-disciplinary open access archive for the deposit and dissemination of scientific research documents, whether they are published or not. The documents may come from teaching and research institutions in France or abroad, or from public or private research centers.

L'archive ouverte pluridisciplinaire **HAL**, est destinée au dépôt et à la diffusion de documents scientifiques de niveau recherche, publiés ou non, émanant des établissements d'enseignement et de recherche français ou étrangers, des laboratoires publics ou privés.



Distributed under a Creative Commons Attribution 4.0 International License

Whispering gallery modes for 3D strain measurement

Yann Lecieux*, Dominique Leduc, Corentin Guigot, Marc François, Cyril Lupi

GeM - Institut de Recherche en Génie Civil et Mécanique - UMR 6183 - Université de Nantes - CNRS - École Centrale de Nantes

Abstract

This paper deals with the use of Whispering Gallery Modes to measure the six components of an homogeneous strain tensor within a sphere undergoing a uniform strain field. The device is a silica sphere in which six WGMs resonate, describing six circles positioned on the sphere's surface in planes perpendicular to the normals of a dodecahedron. The direct model relating the strain to the resonant wavelength variation is established for one circle and then linearised in accordance with the intended application, *i.e.* the realisation of a sensor. The expressions are then generalised to six circles and inverse system computed to obtain an expression for the six components of the strain field as a function of six wavelength shifts of WGMs. Finally, the theoretical performances of the sensor are assessed. The study shows that using a conventional 1 pm resolution detector, the uncertainty on the strain components is, after correction of systematic errors, equal to $2 \mu\varepsilon$.

Keywords: Whispering-gallery modes, Strain, 3D sensor, Optical sensors

1. Introduction

Measuring strain within a structure or material is a complex task due to the nature of the strain. It is a tensor field defined by six independent components at each point of the space. To date, strain sensors are essentially unidirectional and only provide a measurement of
5 one component of the strain tensor in projection along the axial direction of the sensor. Six unidirectional sensors are therefore needed to completely measure the strain at a point in space. Then the problem of the possible non-uniformity of the measured field arises. Since it is not possible to place six sensors at the same point, it is necessary to ensure the uniformity of the strain field in the volume where the different unidirectional sensors are positioned.

*Corresponding author. Email: yann.lecieux@univ-nantes.fr

10 To solve this problem, a sensor concept was recently patented [1]. Its test body is a sphere
crossed by 6 fibres positioned in six directions corresponding to the normals of a dodecahedron
and equipped with a Bragg grating to perform unidirectional strain measurement. Under certain
conditions, the strain is uniform in the sphere [2]. The six fibres therefore measure different
components of the same tensor. The validity of the measurements given by this sensor has been
15 experimentally proven [3, 4].

In its current form, the body measures 4 cm in diameter. This size is well suited for civil
engineering applications but is not suitable for insertion into composite materials or biological
structures. However, the fact of inserting the strain gauges according to diameters in the test
body limits significant miniaturisation of the device. Indeed, it is necessary to have a bonding
20 length of several centimetres for a correct strain transfer from the test body to the fibre [5]–[9].
This requirement defines the minimum diameter of the sphere.

An interesting alternative would be to use a test body cut from a dielectric material as a
medium for light propagation. Indeed, its spherical shape allows it to guide gallery modes [10]–
[13] at its periphery. However, gallery modes are resonant modes: the phase tuning conditions
25 after one revolution mean that there is a relationship between the wavelength of the propagating
mode and the radius of the sphere, its refractive index and the refractive index of the external
medium [14]. Consequently, a sphere radius variation results in a variation of the resonant
wavelength. Measuring the variation of the wavelength can therefore be used to calculate the
strain field within the sphere.

30 Several studies have already demonstrated the link between strain or mechanical loading and
shift of the resonant wavelength. However, all these studies focused on one dimensional strain
analysis in an a priori known direction. In some of them [15]–[19], the gallery modes propagate in
microwire and they shift due to a tensile strain in the axial direction. The aim of the others[20]–
[24] is to develop force sensor with whispering gallery modes in a micro-sphere. The micro-sphere
35 is wedged between two flat plates or a similar arrangement. The force is exerted in the direction
normal to the plates and the contact between the plates and the sphere induce a non homogeneous
strain. The key parameter in these studies is the link between the amplitude of the force in a
given direction and the shift of the wavelength of the whispering gallery mode. The aim of the
study presented here is quite different. The starting point is a micro-sphere embedded in a host
40 material and therefore strained in an unknown manner but in homogeneous strain field. The
problem to solve is to determine the full strain, in all dimensions.

In order to measure strain completely, 6 different gallery modes would have to be used,

following 6 different circles. The question is whether there is a configuration that allows all components of the strain tensor to be measured using these purely tangential measurements, and if so, whether the relationship between the measured wavelengths and the components of the strain tensor is linear over a reasonable range of strains for the sensor to be truly usable in practice.

The objective of this article is to demonstrate that there are linearized relations and an architecture that satisfies these requirements, and then to propose a complete method for the inversion of measurements obtained with this type of sensor. After a brief reminder of the context, the problem statement is presented in section 2. Relationships for calculating strains from the measurement of wavelength shifts will then be established by specifying the necessary approximations to the sections 3 and 4. Then, the optimal architecture of the sensor will be defined in section 5. Finally, the relevance of the approximations with respect to the expected performances in terms of sensitivity and resolution will be discussed in connection with the practical aspects for the implementation of this type of sensor.

2. Problem Statement

Electromagnetic Whispering Gallery Modes propagate in structures with axial symmetry such as discs, torus or spheres [25]–[30]. These are resonant modes with quality-factor as high as 10^9 [31] which makes them suitable for fine measurements of various parameters such as temperature [32], refractive index [14, 33] or biological parameters [29, 34, 35].

The studied structure in this paper is a silica sphere of refractive index n and radius R surrounded by an external medium of index n_{ext} . The spherical coordinate system $(\vec{e}_r, \vec{e}_\theta, \vec{e}_\phi)$ is used for the calculations. From Maxwell equations, it can be seen that two family of modes exist: transverse electric modes (TE) and transverse magnetic modes (TM). In the following, the study will be focused on TE modes. In this case, the electric field in the sphere is given by [36]:

$$\vec{E}_{elec} = A \frac{\psi_\ell(knr)}{knr} \left[j \frac{m P_m^\ell(\cos \theta)}{\sin \theta} \vec{e}_\theta - \frac{\partial P_m^\ell(\cos \theta)}{\partial \theta} \vec{e}_\phi \right] e^{jm\phi} \quad (1)$$

where $k = 2\pi/\lambda$ is the wave number, j the imaginary unit, (r, θ, ϕ) the spherical coordinates, ψ_ℓ a Ricatti-Bessel function of the first kind and P_m^ℓ the associated Legendre polynomials. The parameters ℓ and m are integers such that [37]: $-\ell \leq m \leq \ell$ and $1 < \ell \times \lambda/2\pi R < n/n_{ext}$. ℓ is of the order of 50 for $R = 10 \mu\text{m}$ and 3000 for $R = 500 \mu\text{m}$. For $\ell \gg 1$ the component of the electrical field along \vec{e}_ϕ is negligible [38]. It will then be assumed that the electrical field is purely along \vec{e}_θ .

The continuity of the tangential components of the fields at the interface yields [38, 39]:

$$\frac{n}{n_{\text{ext}}} \frac{\psi'_\ell(knR)}{\psi_\ell(knR)} = \frac{\chi'_\ell(kn_{\text{ext}}R)}{\chi_\ell(kn_{\text{ext}}R)} \quad (2)$$

where χ_ℓ is a Ricatti-Bessel function of the second kind. The exponents prime stand for the derivation with respect to r . This equation gives the wavelengths of the ℓ order modes which can propagate around the sphere. For an unstrained sphere, modes (ℓ, m) are degenerated. The fundamental mode corresponds to $m = \ell$. Schematically, it can be seen as a toroidal beam centered on the equatorial plane ($\theta = \pi/2$) with radial width $\delta r \simeq \lambda$ [37, 40] and angular opening $\delta\theta$ depending on R .

The studied sensor architecture is made of six whispering gallery modes propagating around the sphere along six different circles. The i^{th} mode propagates along a circle perpendicular to the direction \vec{n}_i . The previous field expressions are therefore valid for this mode, provided that the angle θ is measured from the axis carrying \vec{n}_i as shown on figure 1.

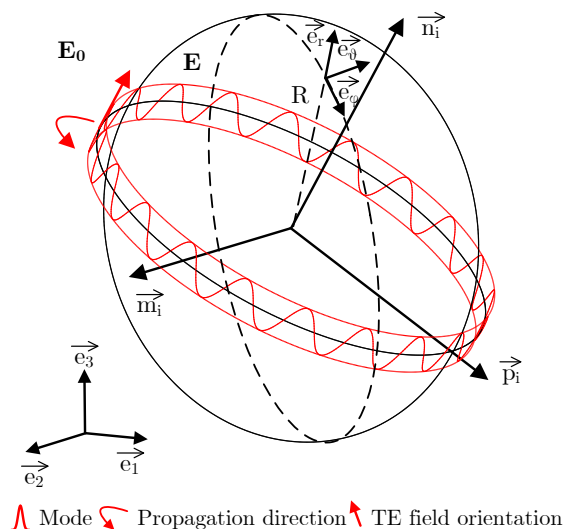


Figure 1: Settings used for the study of WGM

When the sphere is submitted to a uniform strain field \mathbf{E}_0 , in accordance with the intended use as sensor and the assumption of the Eshelby's inclusion theorem, it undergoes a uniform strain \mathbf{E} related to \mathbf{E}_0 by Eshelby's equations [2, 41, 3]. Thus the strains leads to a shift of the wavelength of the i^{th} resonant whispering gallery mode, which can be written as [20]:

$$\frac{\Delta\lambda_i}{\lambda_i} = \frac{\Delta L_i}{L_i} + \frac{\Delta n}{n} - \frac{\ell - m}{2\ell} \Delta(e_i)^2 \quad (3)$$

It depends on three terms: a geometrical term, $\Delta L/L$, that describes the variation of the perimeter of the circle, a photo-elastic term, $\Delta n/n$, that describes the refractive index variation induced by the strain \mathbf{E} and a term depending on the eccentricity of the loop. The latest is of second order in eccentricity and will be neglected (it is by the way strictly null for the fundamental mode). The remaining terms depend on the strain tensor. For each term, this dependence will be explained as well as the calculation allowing to invert the relations obtained.

Before doing so, it is worth considering the limitations of the proposed model. The first concerns the power of the incident beam. Indeed, as the cavity has a high quality factor, a low incident power can lead to a very high energy stored in the cavity and induce non-linear effects or mechanical instabilities. Such effects are observed for threshold powers of a few tens of watts with cavities of quality factor between 10^6 and 10^9 . It is reasonable to take this order of magnitude as the maximum incident power. The second concerns the coupling between modes. In this model it is assumed that the modes are completely decoupled. One way to do this is to interrogate the different modes sequentially, leaving enough time between two interrogations for the energy of the previous mode to be fully dissipated. However, it should be noted that a coupling resulting in an energy transfer between modes with no change in resonant wavelength would be compatible with the proposed method. It would only affect the sensitivity.

3. Linearized relation between the variation of perimeter $\Delta L_i/L$ for a circle of normal \vec{n}_i and the components of the strain tensor \mathbf{E}

The vectors plotted in figure 1 ($\vec{m}_i, \vec{p}_i, \vec{n}_i$) form local orthonormal bases. The components of the strain tensor \mathbf{E} are defined by the equation 4, in the canonical basis ($\vec{e}_1, \vec{e}_2, \vec{e}_3$) and in the local basis ($\vec{m}_i, \vec{p}_i, \vec{n}_i$):

$$\mathbf{E} = \begin{bmatrix} E_{pq} \end{bmatrix}_{(\vec{e}_1, \vec{e}_2, \vec{e}_3)} = \begin{bmatrix} \bar{E}_{pq} \end{bmatrix}_{(\vec{m}_i, \vec{p}_i, \vec{n}_i)} \quad (4)$$

The components of the strain tensor E_{kl} projected in a plane of normal \vec{n}_i are noted E_{kl}^i :

$$E_{ij}^i = P_{ip}^\perp P_{jq}^\perp E_{pq} \quad (5)$$

where P_{kl}^\perp refers to the components of the projector $\mathbf{P}^{[\vec{n}_i^\perp]}$ on the plane of normal \vec{n}_i :

$$\mathbf{P}^{[\vec{n}_i^\perp]} = \mathbf{I} - \vec{n}_i \otimes \vec{n}_i \quad (6)$$

where \mathbf{I} is the identity tensor. In the local basis $(\vec{m}_i, \vec{p}_i, \vec{n}_i)$, the projected tensor noted \mathbf{E}^i of the strain tensor \mathbf{E} has the following components:

$$\mathbf{E}^i = \begin{bmatrix} \overline{E}_{11}^i & \overline{E}_{12}^i & 0 \\ \overline{E}_{12}^i & \overline{E}_{22}^i & 0 \\ 0 & 0 & 0 \end{bmatrix}_{(\vec{m}_i, \vec{p}_i, \vec{n}_i)} . \quad (7)$$

The directions (\vec{m}_i, \vec{p}_i) can be chosen such that they coincide with the \mathbf{E}^i eigenvectors. The associated principal strains are noted as \overline{E}_I^i and \overline{E}_{II}^i . The strain tensor projected onto the \vec{n}_i normal plane is then written as:

$$\mathbf{E}^i = \begin{bmatrix} \overline{E}_I^i & 0 & 0 \\ 0 & \overline{E}_{II}^i & 0 \\ 0 & 0 & 0 \end{bmatrix}_{(\vec{m}_i, \vec{p}_i, \vec{n}_i)} \quad (8)$$

The position vectors of points describing a ring on the sphere surface in the initial and final states are denoted by \vec{x} and \vec{X} respectively. The possible displacement field \vec{u} involves, with a possible additional rigid body motion, the final position vectors \vec{X} as a function of initial position vectors \vec{x} according to:

$$\vec{u} \begin{vmatrix} \overline{E}_I^i x \\ \overline{E}_{II}^i y \\ 0 \end{vmatrix}_{(\vec{m}_i, \vec{p}_i, \vec{n}_i)} \quad \vec{X} \begin{vmatrix} X = (1 + \overline{E}_I^i)x \\ Y = (1 + \overline{E}_{II}^i)y \\ 0 \end{vmatrix}_{(\vec{m}_i, \vec{p}_i, \vec{n}_i)} \quad (9)$$

The points, initially on the circle, satisfy:

$$x^2 + y^2 = R^2 \quad (10)$$

From the equations 9 and 10, it follows:

$$\frac{X^2}{(1 + \overline{E}_I^i)^2} + \frac{Y^2}{(1 + \overline{E}_{II}^i)^2} = R^2 \quad (11)$$

This result shows that a ring, initially circular, takes an elliptical shape under the effect of an homogeneous strain field given by \mathbf{E} . As a consequence, looking for a relation between the perimeter variation of a ring in a plane of normal \vec{n}_i and the components of the strain tensor projected in this same plane \mathbf{E}^i implies to be interested in the calculation of an ellipse perimeter. The latter is obtained following the calculation of an elliptic integral (equation 12):

$$\mathcal{P} = 4 \int_0^{\frac{\pi}{2}} \sqrt{a^2 \cos^2(t) + b^2 \sin^2(t)} dt \quad (12)$$

where a and b are half the lengths of the minor and major axes of the ellipse defined by:

$$a = R(1 + \bar{E}_I^i), \quad b = R(1 + \bar{E}_{II}^i) \quad (13)$$

This equation has no analytical solution. It must therefore be calculated by numerical integration or by rational approximations. Many approximations exist. The choice is made here to express the perimeter variation ΔL_i by using the *Euler* approximation (equation 14) since it is very precise when the ellipse is close to a circle as it is the case under the classical assumption of small perturbations:

$$L + \Delta L_i \approx \pi \sqrt{2(a^2 + b^2)} \quad (14)$$

From this approximation, it is possible to determine the expression of the ring final length $L + \Delta L_i$ as a function of the principal strains ($\bar{E}_I^i, \bar{E}_{II}^i$) and the radius R . Linearising this expression to first order in strain, it comes:

$$L + \Delta L_i = \sqrt{2}\pi \sqrt{R^2(1 + \bar{E}_I^i)^2 + R^2(1 + \bar{E}_{II}^i)^2} \quad (15)$$

$$\simeq 2\pi R \sqrt{1 + \bar{E}_I^i + \bar{E}_{II}^i} \quad (16)$$

$$\frac{\Delta L_i}{2\pi R} \simeq \frac{\bar{E}_I^i + \bar{E}_{II}^i}{2} \quad (17)$$

This expression is the trace of the \mathbf{E}^i tensor in the (\vec{n}_i, \vec{p}_i) basis. This quantity is an invariant, so the following expression is valid whatever the basis:

$$\frac{\Delta L_i}{2\pi R} \simeq \frac{1}{2} \text{trace}(\mathbf{E}^i) \quad (18)$$

100 From the expression 18, it is possible to establish a relation between the perimeter variation and the components of the tensor \mathbf{E} expressed in the $(\vec{e}_1, \vec{e}_2, \vec{e}_3)$ basis. Indeed, the ring length relative variation $\Delta L_i/2\pi R$ is given as a function of the strain tensor components E_{pq} and $P_{pq}^{i\perp}$ the components of the projector $\mathbf{P}^{[\vec{n}_i^\perp]}$, in the canonical basis.

$$\Delta L_i/\pi R = P_{rs}^{i\perp} E_{rs} \quad (19)$$

In expression 19 the double contraction is identified which allows to write:

$$\Delta L_i/\pi R = \mathbf{P}^{[\vec{n}_i^\perp]} : \mathbf{E} \quad (20)$$

105 The equation 20 is a dot product between the two tensors resized as column vectors in Bechterew

basis [42]. Thus the following expression is obtained:

$$\frac{\Delta L_i}{\pi R} = \langle P_{11}^{i\perp} \quad P_{22}^{i\perp} \quad P_{33}^{i\perp} \quad \sqrt{2}P_{23}^{i\perp} \quad \sqrt{2}P_{31}^{i\perp} \quad \sqrt{2}P_{12}^{i\perp} \rangle \left\{ \begin{array}{l} E_{11} \\ E_{22} \\ E_{33} \\ \sqrt{2}E_{23} \\ \sqrt{2}E_{31} \\ \sqrt{2}E_{12} \end{array} \right\} \quad (21)$$

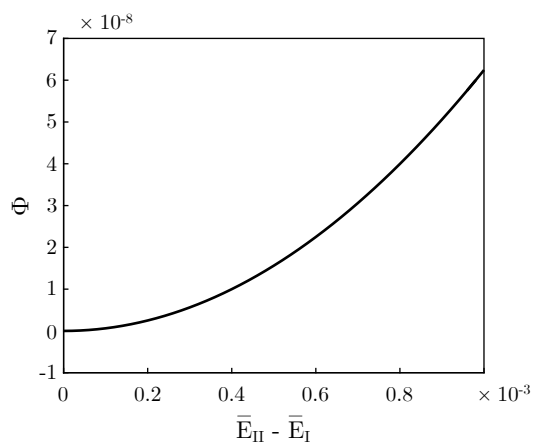


Figure 2: Approximation error in the ellipse perimeter calculation, as a function of the ellipticity $\bar{E}_{II} - \bar{E}_I$.

The model error when estimating the perimeter L^{Approx} of a deformed sphere using equation 18 depends only on the ellipticity of the test body, i.e. the principal strains difference: $\bar{E}_{II} - \bar{E}_I$. To estimate this error, the elliptic integral of the equation 12 is evaluated numerically so as to obtain L^{Num} , the ellipse perimeter to the nearest 10^{-14} in relative value. Figure 2 shows that the relative error, $\Phi = \frac{L^{\text{Approx}} - L^{\text{Num}}}{L^{\text{Num}}}$, reaches at most 6.10^{-8} for an ellipticity of 1.10^{-3} . This value has to be compared to the relative uncertainty on the measured wavelength which is typically of the order of 1 pm/1500 nm or about 6.10^{-7} . The error made by estimating the perimeter length with the approximation 18 (or 21) instead of calculating the perimeter by numerical evaluation of the elliptic integral is much smaller than the measurement error. It is therefore acceptable for the expected range of strains, around 1000×10^{-6} . This approximation will be used in the following since it allows the linearisation of the perimeter variations as a function of the components of the strain tensor with a model error which remains low.

4. Linearized relation between the strain tensor components of \mathbf{E} and the change in refractive index Δn

The photoelastic effects are described by the relation between the changes in the impermeability tensor components \mathbf{B} and the strain tensor \mathbf{E} :

$$\Delta(B_{ij}) = p_{ijkl}E_{kl} \quad , \quad (i, j = 1, 2, 3) \quad (22)$$

where p_{ijkl} are the components of the photoelastic index tensor \mathbb{P}^e . The components of the impermeability tensor and those of the refractive index tensor \mathbf{n} (see [43]) noted n_{ij} are related by the following relation:

$$\Delta(B_{ij}) = \Delta \left(\frac{1}{n_{ij}^2} \right) \quad , \quad (i, j = 1, 2, 3) \quad (23)$$

For an isotropic homogeneous medium, this tensor is expressed by:

$$\mathbf{n} = n\mathbf{I} \quad (24)$$

where n is the refractive index of the medium.

As stated in section 2, the electrical field is along \vec{e}_θ for $\ell \gg 1$. In the following, it will be assumed that this direction can be equated to the normal of the gallery mode propagation plane. Simulations were performed with COMSOL in order to validate this approximation. The 2D axisymmetric system shown on figure 3 was simulated. The system is made of a sphere of refractive index n_1 and radius R (white area on figure 3) embedded in a medium of refractive index n_2 (blue area on figure 3). Waves are absorbed at the external boundary by a $20 \mu\text{m}$ PML (red area on figure 3). Around the dioptr, from $R - 5 \mu\text{m}$ to $R + 5 \mu\text{m}$, a structured mesh made of a $0.5 \mu\text{m}$ squares was used. **This regular arrangement of the finite elements at the interface between the two media is made to avoid creating fictitious dissymmetries in the modes due to dissymmetries of the finite element mesh.** The simulated equation over the whole geometry is :

$$\vec{\nabla} \wedge (\vec{\nabla} \wedge \vec{E}_{\text{elec}}) - k^2 \epsilon_r \vec{E}_{\text{elec}} = \vec{0} \quad (25)$$

The example of figure 3 corresponds to a silica sphere with a radius of $500 \mu\text{m}$. This is the largest size considered in this study.

The figure 4 shows the angular distribution of the component, E_θ^{elec} , of the simulated electrical field of two gallery modes propagating on two different spheres: one with a $100 \mu\text{m}$ radius and the other with a $500 \mu\text{m}$ radius. This figure illustrates the fact that the angular aperture of the

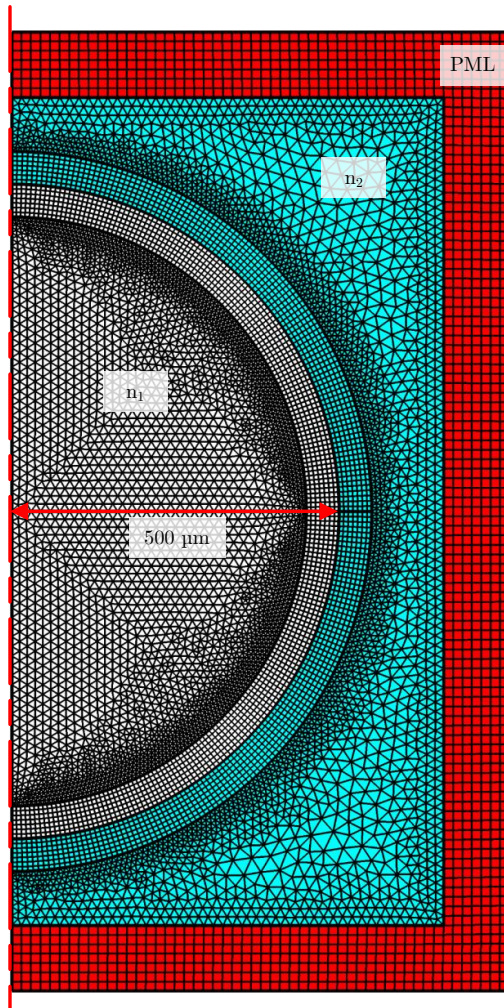


Figure 3: COMSOL modelling of a silica sphere used for WGM simulation.

mode is weak, of the order of 2° for the $500 \mu\text{m}$ sphere. It increases when the radius of the sphere decreases, but remains smaller than 8° for a $100 \mu\text{m}$ sphere. This weak angular aperture justifies that the direction \vec{e}_θ can be equated to the direction \vec{n}_i . The electrical field is therefore assumed to be along \vec{n}_i . As a consequence, it is assumed that the electrical field is just influenced by the refractive index in the direction \vec{n}_i .

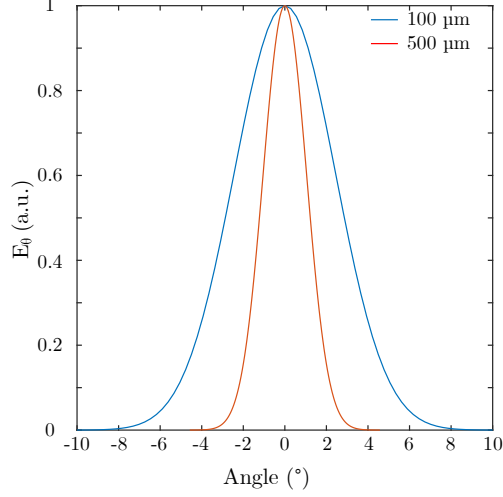


Figure 4: E_θ^{elec} component of a WGM propagating in a silica sphere of $500 \mu\text{m}$ diameter and in a silica sphere of $100 \mu\text{m}$ diameter.

The component ΔB^i of the tensor $\Delta \mathbf{B}$ along a direction \vec{n}_i , is given by:

$$\Delta B^i = \mathbf{P}^{\vec{n}_i} : \Delta \mathbf{B} = \mathbf{P}^{\vec{n}_i} : \mathbb{P}^e : \mathbf{E} \quad (26)$$

where $\mathbf{P}^{\vec{n}_i}$ stands for the projector in the direction \vec{n}_i :

$$\mathbf{P}^{\vec{n}_i} = \vec{n}_i \otimes \vec{n}_i \quad (27)$$

From 23 :

$$\Delta B^i = -\frac{2\Delta n^i}{(n)^3} \quad (28)$$

with Δn^i the refractive index variation in the direction \vec{n}_i . This leads to:

$$\frac{\Delta n^i}{n} = -\frac{(n)^2}{2} \mathbf{P}^{\vec{n}_i} : \mathbb{P}^e : \mathbf{E} \quad (29)$$

This equation, like expression 20, corresponds to a scalar product between the tensors resized as vectors in Bechterew's basis [42]. The system can then be written as:

$$\frac{\Delta n^i}{n} = -\frac{(n)^2}{2} \langle P_{kl}^i \rangle [\mathbb{P}^e] \{E_{pq}\} \quad (30)$$

with the components of the projector:

$$\langle P_{kl}^i \rangle = \langle P_{11}^i \quad P_{22}^i \quad P_{33}^i \quad \sqrt{2}P_{23}^i \quad \sqrt{2}P_{31}^i \quad \sqrt{2}P_{12}^i \rangle \quad (31)$$

the photoelastic index tensor \mathbb{P}^e , in Bechterew [42] basis, is written:

$$[\mathbb{P}^e] = \begin{bmatrix} p_{11} & p_{12} & p_{12} & 0 & 0 & 0 \\ p_{12} & p_{11} & p_{12} & 0 & 0 & 0 \\ p_{12} & p_{12} & p_{11} & 0 & 0 & 0 \\ 0 & 0 & 0 & (p_{11} - p_{12}) & 0 & 0 \\ 0 & 0 & 0 & 0 & (p_{11} - p_{12}) & 0 \\ 0 & 0 & 0 & 0 & 0 & (p_{11} - p_{12}) \end{bmatrix} \quad (32)$$

and $\{E_{pq}\}$ the components of the strain tensor \mathbf{E} written as a column vector:

$$\{E_{pq}\} = \begin{Bmatrix} E_{11} \\ E_{22} \\ E_{33} \\ \sqrt{2}E_{23} \\ \sqrt{2}E_{31} \\ \sqrt{2}E_{12} \end{Bmatrix} \quad (33)$$

In order to assess the approximation consisting in equating \vec{e}_θ to \vec{n}_i , an axisymmetric simulation was carried out with a mode propagating in a plane of normal \vec{e}_3 . A strain E_{11} is imposed along the axis \vec{e}_1 . Since the strain is axisymmetric, the same strain is applied along the \vec{e}_2 axis. The trajectory followed by the mode is always a circle. This simulation allows to test only the hypothesis made on the variation of the optical index. The previous expressions are adapted to this geometrical configuration. Thus the resized projectors as vectors in Bechterew basis [42] are in this case:

$$\mathbf{P}^{[\vec{e}_3^\perp]} = \mathbf{I} - \vec{e}_3 \otimes \vec{e}_3 = \langle 1 \quad 1 \quad 0 \quad 0 \quad 0 \quad 0 \rangle \quad (34)$$

and

$$\mathbf{P}^{[\vec{e}_3]} = \vec{e}_3 \otimes \vec{e}_3 = \langle 0 \quad 0 \quad 1 \quad 0 \quad 0 \quad 0 \rangle \quad (35)$$

According to the equations, 3 and 30 :

$$\frac{\Delta L}{L} = \frac{E_{11} + E_{22}}{2} ; \quad \frac{\Delta n}{n} = -\frac{n^2}{2}(p_{12}E_{11} + p_{12}E_{22} + p_{11}E_{33}) \quad (36)$$

By adding the geometric and photoelastic effect, the wavelength shift is written:

$$\frac{\Delta \lambda}{\lambda} = \frac{E_{11} + E_{22}}{2} - \frac{n^2}{2}(p_{12}E_{11} + p_{12}E_{22} + p_{11}E_{33}) \quad (37)$$

For the axisymmetric simulation with $E_{11} = E_{22}$, this expression becomes:

$$\frac{\Delta\lambda}{\lambda} = E_{11} - \frac{n^2}{2}(2p_{12}E_{11} + p_{11}E_{33}) \quad (38)$$

The difference between the simulation results performed using COMSOL and considered as the reference and the simplified analytical expression is given in Figure 5 as a function of the diameter of the sphere. As expected, the larger the sphere, the lower the angular aperture and thus the lower the difference between the analytical approximation and the numerical simulation. For a 100 μm sphere, the difference is of the order of 4%, whereas for a 500 μm sphere, it is lower than 1%.

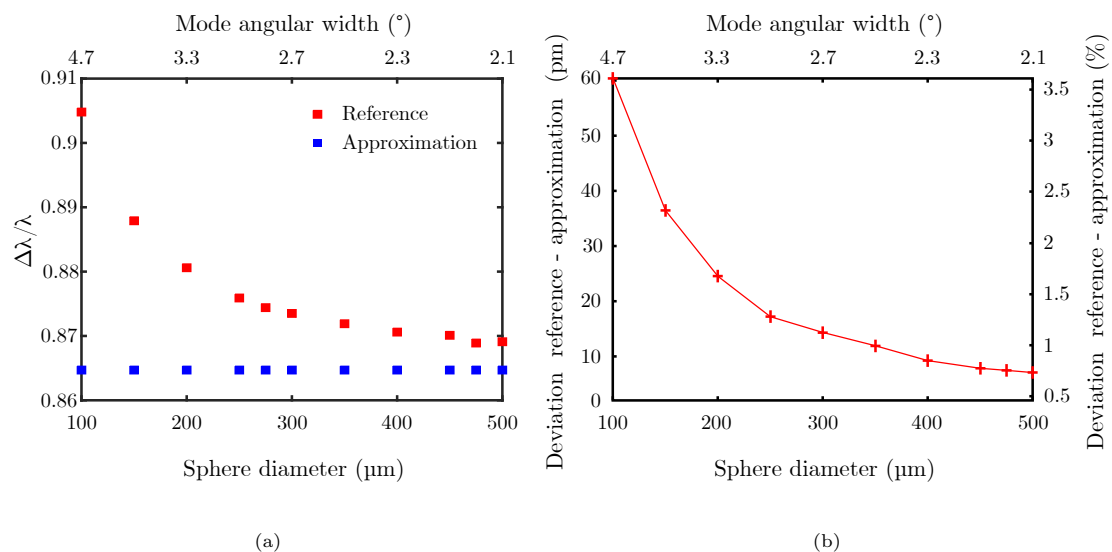


Figure 5: (a) Relative wavelength shift calculated by simulation or using the simplified analytical expression as a function of the diameter of the sphere (for $E_{11} = 2000 \cdot 10^{-6}$, $n = 1.45$ and $p_{12} = 0.27$). (b) Difference between the wavelength variations calculated by simulation or using the simplified analytical expression as a function of the diameter of the sphere.

The approximated expression 30 can therefore be used. It enables a linear relation between the refraction index variation and the strain tensor components with an error that remains low provided that the sphere is not too small.

5. Towards a strain measurement device using WGM propagation along 6 different circles

The choice of the measurement planes which defines the components of the normals and therefore the components of the projectors $P_{kl}^{i\perp}$ and P_{kl}^i must be made in such a way that the

145 system is invertible. Among all the combinations, it is preferable to choose a regular distribution of the planes in space so that the behaviour of the sensor is not affected by its orientation with respect to the main directions of the strain field \mathbf{E}_0 . The best solution is to measure perimeter variations in planes perpendicular to the normals of a dodecahedron:

$$\begin{aligned}
\vec{n}_1 &= (0, \varphi, 1)/\sqrt{2+\varphi} \\
\vec{n}_2 &= (0, \varphi, -1)/\sqrt{2+\varphi} \\
\vec{n}_3 &= (1, 0, \varphi)/\sqrt{2+\varphi} \\
\vec{n}_4 &= (1, 0, -\varphi)/\sqrt{2+\varphi} \\
\vec{n}_5 &= (\varphi, 1, 0)/\sqrt{2+\varphi} \\
\vec{n}_6 &= (\varphi, -1, 0)/\sqrt{2+\varphi}
\end{aligned} \tag{39}$$

where $\varphi = (1 + \sqrt{5})/2$ is the golden ratio. The architecture representing this solution is shown in Figure 6. With this configuration of sensors, the system 21 becomes:

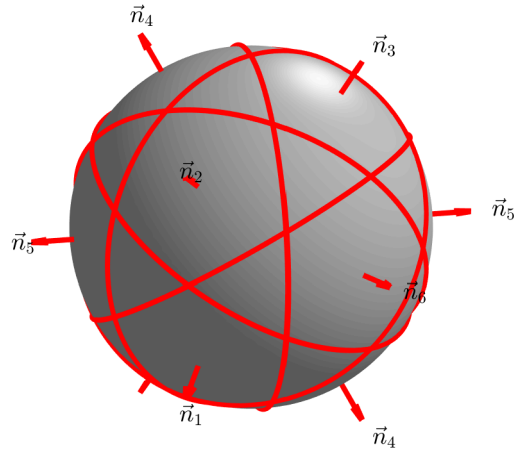


Figure 6: Distribution of the measurement perimeters on a 6-ring sensor, as also presented in [44] or in [45] for a hollow structure.

$$\left\{ \frac{\Delta L_i}{L_i} \right\} = \frac{1}{2} \left\{ \frac{\Delta L_i}{\pi R} \right\} = \frac{1}{2} [M_L] \{E_i\} \tag{40}$$

where the matrix $[M_L]$, according to the property $\varphi^2 - 1 = \varphi$, is written:

$$[M_L] = \frac{1}{2 + \varphi} \begin{bmatrix} 2 + \varphi & 1 & 1 + \varphi & -\sqrt{2}\varphi & 0 & 0 \\ 2 + \varphi & 1 & 1 + \varphi & \sqrt{2}\varphi & 0 & 0 \\ 1 + \varphi & 2 + \varphi & 1 & 0 & -\sqrt{2}\varphi & 0 \\ 1 + \varphi & 2 + \varphi & 1 & 0 & \sqrt{2}\varphi & 0 \\ 1 & 1 + \varphi & 2 + \varphi & 0 & 0 & -\sqrt{2}\varphi \\ 1 & 1 + \varphi & 2 + \varphi & 0 & 0 & \sqrt{2}\varphi \end{bmatrix} \quad (41)$$

150 and

$$\{E_i\} = \begin{Bmatrix} E_{11} \\ E_{22} \\ E_{33} \\ E_{23} \\ E_{31} \\ E_{12} \end{Bmatrix} \quad (42)$$

A similar relationship can be established between the components of the strain tensor and the wavelength variations resulting from the index variations $\frac{\Delta n^i}{n}$ (see equations 30, 31 and 32).

$$\begin{Bmatrix} \frac{\Delta n^1}{n^1} \\ \frac{\Delta n^2}{n^2} \\ \frac{\Delta n^3}{n^3} \\ \frac{\Delta n^4}{n^4} \\ \frac{\Delta n^5}{n^5} \\ \frac{\Delta n^6}{n^6} \end{Bmatrix} = -\frac{(n)^2}{2} \begin{bmatrix} \\ \\ \\ \\ \\ \\ \end{bmatrix} \begin{bmatrix} \\ \\ \\ \\ \\ \\ \end{bmatrix} \begin{Bmatrix} E_{11} \\ E_{22} \\ E_{33} \\ E_{23} \\ E_{31} \\ E_{12} \end{Bmatrix} \quad (43)$$

with $[M_n]$, the matrix composed by the projectors $\mathbf{P}^{\vec{n}_i}$ along the 6 normals \vec{n}_i , i.e.:

$$[M_n] = \frac{1}{(2 + \varphi)} \begin{bmatrix} 0 & 1 + \varphi & 1 & \sqrt{2}\varphi & 0 & 0 \\ 0 & 1 + \varphi & 1 & -\sqrt{2}\varphi & 0 & 0 \\ 1 & 0 & 1 + \varphi & 0 & \sqrt{2}\varphi & 0 \\ 1 & 0 & 1 + \varphi & 0 & -\sqrt{2}\varphi & 0 \\ 1 + \varphi & 1 & 0 & 0 & 0 & \sqrt{2}\varphi \\ 1 + \varphi & 1 & 0 & 0 & 0 & -\sqrt{2}\varphi \end{bmatrix} \quad (44)$$

In the equations 40 and 43, the writing in tensor basis is no longer used. The multipliers $\sqrt{2}$ of the E_{ij} terms are integrated in the matrices $[M_L]$ and $[M_n]$ in order to obtain a relation between the components of the strain tensor and the WGM shifts that can be easily inverted. Finally, this relationship can be written as:

$$\left\{ \frac{\Delta\lambda_i}{\lambda} \right\} = \frac{[M_L] - n^2[M_n][\mathbb{P}^e]}{2} \{E_i\} = \frac{[M]}{2} \{E_i\}, \quad i \in 1..6 \quad (45)$$

where $[M]$ has the following form:

$$[M] = \begin{bmatrix} M_1 & M_2 & M_3 & -M_4 & 0 & 0 \\ M_1 & M_2 & M_3 & M_4 & 0 & 0 \\ M_3 & M_1 & M_2 & 0 & -M_4 & 0 \\ M_3 & M_1 & M_2 & 0 & M_4 & 0 \\ M_2 & M_3 & M_1 & 0 & 0 & -M_4 \\ M_2 & M_3 & M_1 & 0 & 0 & M_4 \end{bmatrix} \quad (46)$$

with :

$$\begin{aligned} M_1 &= 1 - n^2 p_{12} \\ M_2 &= \frac{1 - n^2[(1 + \varphi)p_{11} + p_{12}]}{2 + \varphi} \\ M_3 &= \frac{(1 + \varphi)(1 - n^2 p_{12}) - n^2 p_{11}}{2 + \varphi} \\ M_4 &= \frac{\sqrt{2}\varphi}{2 + \varphi} [1 + n^2(p_{11} - p_{12})] \end{aligned} \quad (47)$$

To obtain the components of the strain tensor from the resonant wavelength variations, the relationship 45 must be inverted:

$$\{E_i\} = 2[M]^{-1} \left\{ \frac{\Delta\lambda_i}{\lambda} \right\}, \quad i \in 1..6 \quad (48)$$

which is only possible if the determinant D of the matrix $[M]$ is not zero. This determinant is as follows:

$$D = -8M_4^3(M_1^3 + M_2^3 + M_3^3 - 3M_1M_2M_3) = \frac{32\sqrt{2}\varphi^5}{(\varphi + 2)^5} P_1(p_{11}, p_{12}, n)^5 P_2(p_{11}, p_{12}, n) \quad (49)$$

with

$$\begin{aligned} P_1(p_{11}, p_{12}, n) &= n^2(p_{11} - p_{12}) + 1 \\ P_2(p_{11}, p_{12}, n) &= n^2(p_{11} + 2p_{12}) - 2 \end{aligned} \quad (50)$$

The determinant therefore becomes zero when $P_1 = 0$ or $P_2 = 0$. This means that for some sets of parameters $\{p_{11}, p_{12}, n\}$, the effect of the geometry change $\Delta L/L$ on the wavelength

155 shift of WGM is partially compensated by the photoelastic effect $\Delta n/n$. The coloured maps in Figure 7 represent the sets of parameters for which these polynomials are zero. These are the configurations to be avoided for the realisation of a 3D strain sensor.

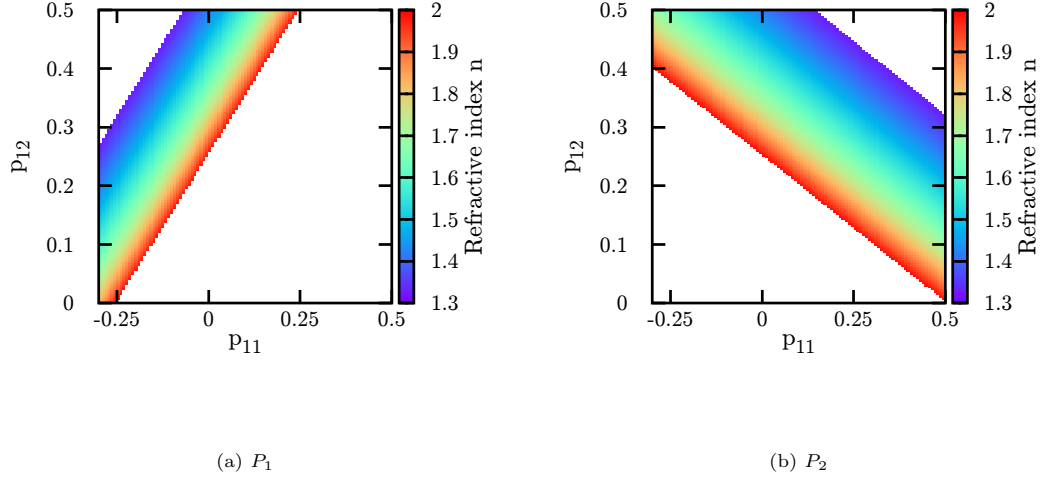


Figure 7: In colour are represented the points of the space of parameters $\{p_{11}, p_{12}, n\}$ for which the determinant of the matrix $[M]$ is zero. The color-bar indicates the value of the index n to be avoided for a given set of parameters $\{p_{11}, p_{12}\}$.

The matrix $[M]^{-1}$, if it exists, has the following form:

$$[M]^{-1} = \begin{bmatrix} m_1 & m_1 & m_3 & m_3 & m_2 & m_2 \\ m_2 & m_2 & m_1 & m_1 & m_3 & m_3 \\ m_3 & m_3 & m_2 & m_2 & m_1 & m_1 \\ m_4 & -m_4 & 0 & 0 & 0 & 0 \\ 0 & 0 & m_4 & -m_4 & 0 & 0 \\ 0 & 0 & 0 & 0 & m_4 & -m_4 \end{bmatrix} \quad (51)$$

where:

$$\begin{aligned}
m_1 &= \frac{4M_4^3}{D}(M_2M_3 - M_1^2) \\
m_2 &= \frac{4M_4^3}{D}(M_1M_3 - M_2^2) \\
m_3 &= \frac{4M_4^3}{D}(M_1M_2 - M_3^2) \\
m_4 &= -\frac{1}{2M_4}
\end{aligned} \tag{52}$$

6. Sensitivity analysis

The objective of this section is to study the influence of the different parameters involved in the measurement on the accuracy of the measurement. First of all, it should be reminded that the radius of the sphere conditions the validity of the approximation as shown on the figure 5. This approximation leads to a systematic error that must be corrected before analysis.

Material	n	p_{11}	p_{12}	S_1 ($pm/\mu\varepsilon$)	S_2 ($pm/\mu\varepsilon$)	S_3 ($pm/\mu\varepsilon$)	S_4 ($pm/\mu\varepsilon$)
Fused silica [46]	1.458	0.121	0.27	0.319	-0.051	0.178	0.324
Doped silica [47]	1.447	0.113	0.252	0.354	-0.030	0.207	0.336
PMMA [48]	1.49	0.3	0.28	0.28	-0.28	0.07	0.49
Diamond [49]	2.4	0.12	-0.32	2.13	0.21	1.4	1.68
Silicon Carbide [50]	2.6	-0.15	0.04	0.547	0.701	0.606	-0.134

Table 1: Optical constants and sensitivities of different materials

From an experimental point of view, the measurement consists in determining the wavelength of a dip in the intensity of the light transmitted by the fiber which serves as a coupler. The accuracy of the measurement therefore depends on the depth and width of the dip. With standard detectors, a depth of -45 dBm is enough to detect the dip. The coupling has to be adjusted to insure this minimal depth. The typical wavelength resolution is then of the order of 1 pm for a width of a few hundred pm. This can easily be achieved since it corresponds to a quality factor of the order of 10^5 . In this framework, the sensibility of the measurement method is given by the components of the matrix $[M]$ of equation 47. These components depend on the

refractive index and on the components of the photoelastic tensor. Few values of the latter are available in the literature. They depend on the material and vary slowly with wavelength in the transparency zone. For example the photoelastic constants of fused silica exhibit a 10% variation between 650 nm and 230 nm, with a more pronounced increase in the vicinity of UV [51, 52]. The table 1 synthesizes these parameters for different materials such as $p_{44} \simeq (p_{11} - p_{12})/2$ using the classical Voight notation found in the literature, together with the associated sensitivities. To better match the experimental protocol, the quantities $S_i = \lambda M_i/2$ (with $\lambda = 1500 \text{ nm}$) are reported in this table since they directly give the wavelength shift induced by the strain and associated to the component M_i . More precisely, from equation 45, it can be seen that the wavelength shift measured for the mode 1 is given by:

$$\Delta\lambda_1 = S_1 E_{11} + S_2 E_{22} + S_3 E_{33} - S_4 E_{23} + 0 \times E_{31} + 0 \times E_{12} \quad (53)$$

The modes 1 is then completely insensitive to shear E_{31} and E_{12} , whatever the material. In the same way, mode 2 is insensitive to shear E_{31} and E_{12} , mode 3 and 4 to shear E_{23} and E_{12} , and modes 5 and 6 to shear E_{23} and E_{31} . For fused or doped silica, modes 1 and 2 are ten times less sensitive to strain along direction \vec{e}_2 than to strain along the other two directions. Similar observations can be made for the other modes with direction \vec{e}_3 for modes 3 and 4 and direction \vec{e}_1 for modes 5 and 6. For the considered materials, the best sensitivities are expected for diamond. In a general manner, it can be seen from equation 47 that the sensitivities increase with n^2 .

The last step is to determine the influence of the uncertainties on the measured wavelengths on the uncertainties on the components of the strain tensor. A statistical study can be done as a first approach. A strain state is defined by randomly chosen the strain components in the $[-1000.10^{-6}, +1000.10^{-6}]$ range. Then, the expected wavelength shifts for the 6 gallery modes are computed with the help of equation 45. In order to simulate the noise, a random value uniformly distributed in the range $[-N_{\text{oise}}, +N_{\text{oise}}]$ is added to each shift and then the strain components corresponding to this noisy set are computed with equation 48. This is repeated a thousand times. It is then observed that, for each component, the difference between the mean value of the noisy strain and the correct one is one or two order less than the standard deviation of the distribution of noisy strain. This standard deviation can then be used as uncertainty. Finally, ten thousands states of strain were considered. An example of the distribution of the uncertainties on the component E_1 is shown on figure 8 for a doped silica sphere and a noise equal to 1 pm. The mean value of this distribution corresponds to the uncertainty on E_{11} .

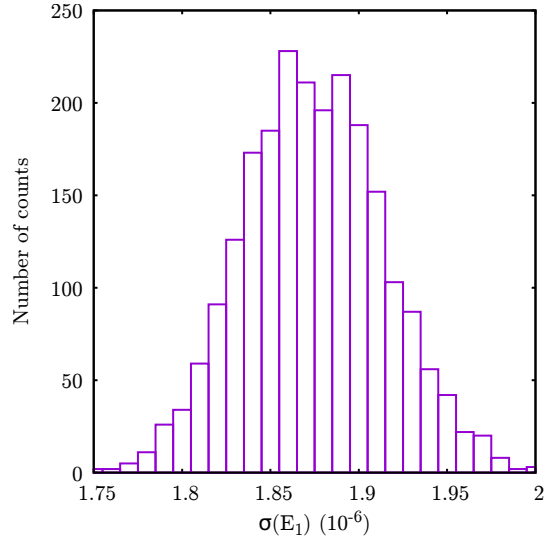


Figure 8: Distribution of uncertainties on E_1 for fused silica and $N_{\text{oise}} = 1$ pm

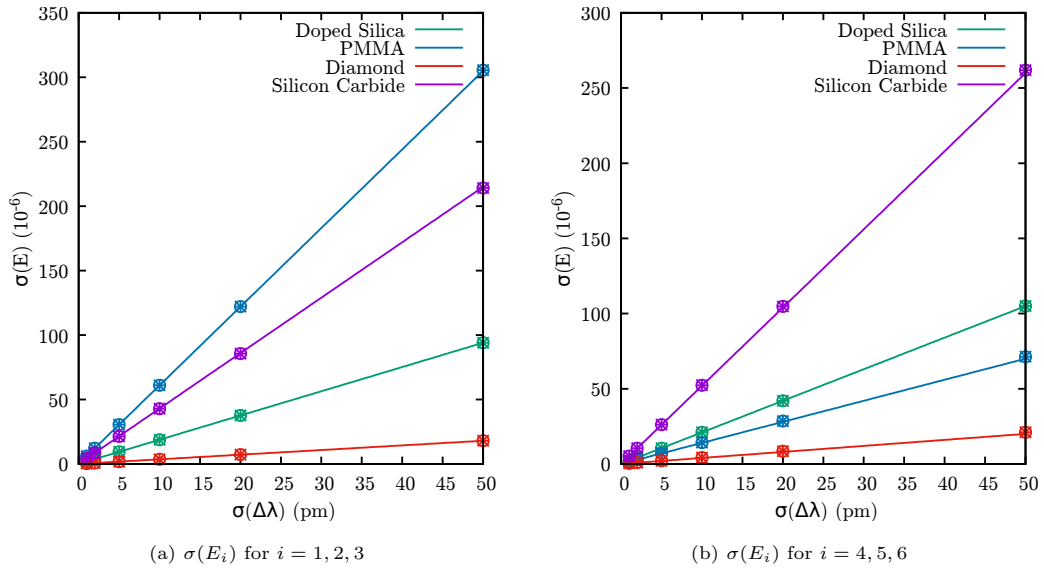


Figure 9: Uncertainties on strain as a function of uncertainties on wavelength shifts

The figure 9 shows the variation of the uncertainties on the strain with noise on wavelength for different materials. The uncertainties of modes 1, 2 and 3 behave in exactly the same way. So do the uncertainties of modes 4, 5 and 6. All vary linearly with the uncertainty on the wavelength shift, with a slope that depends on the material. This can be easily explained. Indeed, the wavelength measurements will be made with a spectrum analyser or a tunable source. Whatever the device used, it will not be necessary to change the calibration in the range of strains considered. It is therefore legitimate to consider the measured wavelength as the sum of the correct wavelength and a random noise that depends only on the detection system:

$$\{\Delta\lambda\}_{\text{meas}} = \{\Delta\lambda\}_{\text{th}} + \{N_{\text{oise}}\} \quad (54)$$

then:

$$\{E\}_{\text{meas}} = 2[M]^{-1}\{\Delta\lambda/\lambda\}_{\text{meas}} = 2[M]^{-1}\{\Delta\lambda/\lambda\}_{\text{th}} + 2[M]^{-1}\{N_{\text{oise}}/\lambda\} = \{E\}_{\text{th}} + \{E\}_{\text{err}} \quad (55)$$

The error made on the strain is simply that:

$$\{E\}_{\text{err}} = 2[M]^{-1}\{N_{\text{oise}}/\lambda\} \quad (56)$$

Using the classical law of uncertainty composition:

$$\sigma(E_i) = \sqrt{\sum_{j=0}^6 \left(\frac{\partial E_i}{\partial \lambda_j}\right)^2 \frac{\sigma^2(\Delta\lambda_j)}{\lambda_j^2}} \quad (57)$$

and assuming that the wavelength uncertainty is the same on all measurement channels: $\sigma(\Delta\lambda_j) = \sigma(\Delta\lambda) \forall j$, it comes:

$$\sigma(E_i) = s \sigma(\Delta\lambda) \quad \text{with} \quad s = \begin{cases} s_{123} = \frac{2\sqrt{2}}{\lambda_0} \sqrt{(m_1^2 + m_2^2 + m_3^2)} & \text{for } i = 1, 2, 3 \\ s_{456} = \frac{2\sqrt{2}}{\lambda_0} m_4 & \text{for } i = 4, 5, 6 \end{cases} \quad (58)$$

where λ_0 is the resonant wavelength of the undeformed sphere.

185 The coefficients s_{123} and s_{456} for the materials considered in this study are reported on table 2 and used to draw the straight lines in figure 9. They range from $0.4 \mu\epsilon/pm$ for the diamond to $6 \mu\epsilon/pm$ for the PMMA and are close to $2 \mu\epsilon/pm$ for the silica. To put it in perspective, with a silica sphere, and with a conventional detector of resolution equal to 1 pm, the error on the strain components is, after correction of systematic errors, of the order of $2 \mu\epsilon$. This means that
190 this sensor is capable to give the six components of the strain tensor with an uncertainty of the same order of that of a classical strain gauge which only gives the strain along one direction.

Material	s_{123} ($\mu\epsilon/pm$)	s_{456} ($\mu\epsilon/pm$)
Fused silica [46]	2.	2.2
Doped silica [47]	1.9	2.1
PMMA [48]	6.1	1.4
Diamond [49]	0.4	0.4
Silicon Carbide [50]	4.3	5.2

Table 2: Uncertainty coefficients

7. Conclusion

In this paper, the realization of a 3D strain sensor with a silica sphere as test body and 6 gallery modes as unidirectional strain gauges is studied. The direct model relating the strain to the resonant wavelength variation is described and linearised. The inversion method is then presented.

The direct linear model is established by considering a single whispering gallery mode. Two phenomena combine to change the resonant wavelength: a geometrical effect inducing a variation in perimeter and a photoelastic effect inducing a variation in refractive index. From a geometric point of view, when the sphere deforms, the perimeter of the circle covered by the gallery mode changes and may become an ellipse. The corresponding perimeter variation can be approximated using the trace of the strain tensor. The relative error using this approximation is less than 10^{-7} for a strain $(\bar{E}_{II} - \bar{E}_I)$ less than $1000 \mu\epsilon$. Taking into account the photo-elastic effect is more delicate. To establish a linear relationship between the strain and the wavelength variation, it is necessary to use an approximation where the electric field of the wave is purely perpendicular to the plane in which the mode propagates. This approximation is more accurate as the radius of the sphere increases. The relative error on the wavelength variation is of the order of 5 % for a $100 \mu\text{m}$ sphere and falls below 1% for a $500 \mu\text{m}$ sphere. Beyond the sensor application presented here, this model can be useful to correct any measurement for the effects of strain when it is not the quantity of interest.

The direct model was then applied to 6 gallery modes regularly distributed on the sphere to obtain a matrix relationship between the wavelength variation and the strain. This system is inverted and the components of the matrix allowing to obtain the 6 components of the strain tensor from the 6 wavelength measurements were given explicitly. In practice, this matrix

215 contains only 4 different components and many zeros, so that the shear components depend
on only two wavelength measurements along two different circles, while the other components of
the strain tensor depend on all 6 wavelength measurements.

Finally, in terms of sensitivity, it has been shown that the uncertainty in $[\mu\varepsilon]$ on the components
of the strain tensor is twice the uncertainty in $[\text{pm}]$ on the wavelength measurement. To give an
220 order of magnitude, an uncertainty of 1 pm on the wavelength leads to an uncertainty of $2 \mu\varepsilon$,
which makes the performance of the proposed sensor consistent with that of conventional fibre
optic sensors.

From an experimental point of view, it must be recognised that the development of such
a sensor is likely to be very complicated. The question of mode injection is a major problem,
225 especially as six modes have to be excited. However, there are already signs that this is possible.
For example, the system described by Yan [53] where the sphere is covered by a drop of resin
which also traps the tap could be used with six tapers. Similarly, the system described by
Weigel [23] where a droplet of DDI solved in ethanol is inserted with help of a syringe in a
silicone matrix could be used with 6 optical fibers fixed in the matrix. In both cases, the final
230 size of the sensor, of the order of few hundreds of μm , would prohibits its use in biology at the
cell level. But it could find applications in composites materials [54, 55] or bonded joints [56, 57]
where the measurement of shrinkage is of major importance.

In any case, as soon as the sensor can be manufactured, the analysis method described in
this article can be used as is.

235 **Acknowledgment**

This work has been supported by a grant from the Région Pays de la Loire within the
framework of the SMOG Project.

References

- [1] M. L. M. François, Y. Lecieux, C. Lupi, D. Leduc, Strain measuring device (Patent
240 FR3003346A1. Sep. 2014).
- [2] J. D. Eshelby, The Determination of the Elastic Field of an Ellipsoidal Inclusion, and
Related Problems, Proceedings of the Royal Society of London A: Mathematical, Physical
and Engineering Sciences 241 (1226) (1957) 376–396. doi:10.1098/rspa.1957.0133.
URL <http://rspa.royalsocietypublishing.org/content/241/1226/376>

- 245 [3] M. L. M. François, Y. Lecieux, D. Leduc, C. Lupi, E. Rozière, An Embedded 3D Strain
Tensor Sensor Based on the Eshelby's Inclusion, *Experimental Mechanics* 57 (5) (2017)
801–811. doi:10.1007/s11340-017-0266-2.
URL <https://link.springer.com/article/10.1007/s11340-017-0266-2>
- [4] Y. Lecieux, E. Roziere, C. Lupi, D. Leduc, M. L. M. François, Towards a 3d shrinkage
250 measurement in concrete using an embedded strain sensor, *Smart Materials and Structures*
27 (2018) 105032.
- [5] K. T. Wan, C. K. Y. Leung, N. G. Olson, Investigation of the strain transfer for surface-
attached optical fiber strain sensors, *Smart Materials and Structures* 17 (3) (2008) 035037,
publisher: IOP Publishing. doi:10.1088/0964-1726/17/3/035037.
255 URL <https://doi.org/10.1088/0964-1726/17/3/035037>
- [6] S.-C. Her, C.-Y. Huang, Effect of Coating on the Strain Transfer of Optical Fiber Sensors,
Sensors 11 (7) (2011) 6926–6941, number: 7 Publisher: Molecular Diversity Preservation
International. doi:10.3390/s110706926.
URL <https://www.mdpi.com/1424-8220/11/7/6926>
- 260 [7] X. Feng, J. Zhou, C. Sun, X. Zhang, F. Ansari, Theoretical and Experimental Investigations
into Crack Detection with BOTDR-Distributed Fiber Optic Sensors, *Journal of Engineering
Mechanics* 139 (12) (2013) 1797–1807, publisher: American Society of Civil Engineers. doi:
10.1061/(ASCE)EM.1943-7889.0000622.
URL <https://ascelibrary.org/doi/abs/10.1061/%28ASCE%29EM.1943-7889.0000622>
- 265 [8] I. Alj, M. Quiertant, A. Khadour, Q. Grando, B. Terrade, J.-C. Renaud, K. Benzarti,
Experimental and Numerical Investigation on the Strain Response of Distributed Optical
Fiber Sensors Bonded to Concrete: Influence of the Adhesive Stiffness on Crack Monitoring
Performance, *Sensors* 20 (18) (2020) 5144, number: 18 Publisher: Multidisciplinary Digital
Publishing Institute. doi:10.3390/s20185144.
270 URL <https://www.mdpi.com/1424-8220/20/18/5144>
- [9] A. Billon, J.-M. Henault, M. Quiertant, F. Taillade, A. Khadour, R.-P. Martin, K. Benzarti,
Quantitative Strain Measurement with Distributed Fiber Optic Systems: Qualification of
a Sensing Cable Bonded to the Surface of a Concrete Structure, in: V. Le Cam, L. Mevel,
F. Schoefs (Eds.), *EWSHM - 7th European Workshop on Structural Health Monitoring*,

- 275 IFFSTTAR, Inria, Université de Nantes, Nantes, France, 2014.
URL <https://hal.inria.fr/hal-01022049>
- [10] G. Mie, Beiträge zur Optik trüber Medien, speziell kolloidaler Metallösungen, *Annalen der Physik* 330 (3) (1908) 377–445. doi:10.1002/andp.19083300302.
- [11] C. C. Lam, P. T. Leung, K. Young, Explicit asymptotic formulas for the positions, widths,
280 and strengths of resonances in Mie scattering, *Journal of the Optical Society of America B Optical Physics* 9 (1992) 1585–1592. doi:10.1364/JOSAB.9.001585.
- [12] S. Schiller, Asymptotic expansion of morphological resonance frequencies in Mie scattering, *Applied Optics* 32 (12) (1993) 2181–2185. doi:10.1364/AO.32.002181.
- [13] G. Righini, Y. Dumeige, P. Feron, M. Ferrari, G. Nunzi Conti, D. Ristić, S. Soria,
285 Whispering gallery mode microresonators: Fundamentals and applications, *La Rivista del Nuovo Cimento* 34 (2011) 435. doi:10.1393/ncr/i2011-10067-2.
- [14] N. M. Hanumegowda, C. J. Stica, B. C. Patel, I. White, X. Fan, Refractometric sensors based on microsphere resonators, *Applied Physics Letters* 87 (20) (2005) 201107.
- [15] C. Linslal, M. Kailasnath, S. Mathew, T. Nideep, P. Radhakrishnan, V. Nampoori,
290 C. Vallabhan, Tuning whispering gallery lasing modes from polymer fibers under tensile strain, *Optics letters* 41 (3) (2016) 551–554.
- [16] V. Kavungal, G. Farrell, Q. Wu, A. K. Mallik, Y. Semenova, A packaged whispering gallery mode strain sensor based on a polymer-wire cylindrical micro resonator, *Journal of Lightwave Technology* 36 (9) (2017) 1757–1765.
- [17] J. Lu, C. Xu, F. Li, Z. Yang, Y. Peng, X. Li, M. Que, C. Pan, Z. L. Wang, Piezoelectric
295 effect tuning on zno microwire whispering-gallery mode lasing, *ACS nano* 12 (12) (2018) 11899–11906.
- [18] Y. Peng, J. Lu, D. Peng, W. Ma, F. Li, Q. Chen, X. Wang, J. Sun, H. Liu, C. Pan, Dynamically modulated gan whispering gallery lasing mode for strain sensor, *Advanced
300 Functional Materials* 29 (42) (2019) 1905051.
- [19] A. Lee, S.-K. Lee, S. H. Lee, Simultaneous temperature and strain sensing with hybrid resonator of fiber bragg grating and whispering gallery resonator, *IEEE Sensors Journal* 20 (6) (2019) 2962–2966.

- [20] V. S. Ilchenko, P. S. Volikov, V. L. Velichansky, F. Treussart, V. Lefèvre-Seguin,
305 J. M. Raimond, S. Haroche, Strain-tunable high-Q optical microsphere resonator, *Optics Communications* 145 (1) (1998) 86–90. doi:10.1016/S0030-4018(97)00439-2.
URL <http://www.sciencedirect.com/science/article/pii/S0030401897004392>
- [21] T. Ioppolo, U. K. Ayaz, M. V. Ötügen, High-resolution force sensor based on morphology
dependent optical resonances of polymeric spheres, *Journal of Applied Physics* 105 (1) (2009)
310 013535, publisher: American Institute of Physics. doi:10.1063/1.3054338.
URL <https://aip.scitation.org/doi/full/10.1063/1.3054338>
- [22] N. Q. Nguyen, N. Gupta, T. Ioppolo, M. V. Ötügen, Whispering gallery mode-based micro-
optical sensors for structural health monitoring of composite materials, *Journal of materials
science* 44 (6) (2009) 1560–1571.
- [23] T. Weigel, C. Esen, G. Schweiger, A. Ostendorf, Whispering gallery mode pressure sensing,
315 in: *Optical Sensing and Detection II*, Vol. 8439, International Society for Optics and
Photonics, 2012, p. 84390T.
- [24] H. Wagner, H. Schmitzer, J. Lutti, P. Borri, W. Langbein, Effects of uniaxial pressure on
polar whispering gallery modes in microspheres, *Journal of Applied Physics* 113 (24) (2013)
320 243101.
- [25] A. N. Oraevsky, Whispering-gallery waves, *Quantum electronics* 32 (5) (2002) 377.
- [26] T. J. A. Kippenberg, *Nonlinear Optics in Ultra-High-Q Whispering-Gallery Optical
Microcavities*, phd, California Institute of Technology (2004). doi:10.7907/T5B6-9R14.
URL <https://resolver.caltech.edu/CaltechETD:etd-06072004-085555>
- [27] A. Morand, K. Phan-Huy, Y. Desieres, P. Benech, Analytical study of the microdisk’s
325 resonant modes coupling with a waveguide based on the perturbation theory, *Journal of
lightwave technology* 22 (3) (2004) 827.
- [28] A. Schweinsberg, S. Hocdé, N. N. Lepeshkin, R. W. Boyd, C. Chase, J. E. Fajardo, An
environmental sensor based on an integrated optical whispering gallery mode disk resonator,
330 *Sensors and Actuators B: Chemical* 123 (2) (2007) 727–732.
- [29] G. C. Righini, S. Soria, Biosensing by wgm microspherical resonators, *Sensors* 16 (6) (2016)
905.

- [30] G. C. Righini, *Glass Micro-and Nanospheres: Physics and Applications*, CRC Press, 2019.
- [31] D. Vernooy, V. S. Ilchenko, H. Mabuchi, E. Streed, H. Kimble, High-q measurements of fused-silica microspheres in the near infrared, *Optics letters* 23 (4) (1998) 247–249.
- [32] Y. Zhi, A. Meldrum, Tuning a microsphere whispering-gallery-mode sensor for extreme thermal stability, *Applied Physics Letters* 105 (3) (2014) 031902.
- [33] S. Pang, R. E. Beckham, K. E. Meissner, Quantum dot-embedded microspheres for remote refractive index sensing, *Applied physics letters* 92 (22) (2008) 221108.
- [34] S. Soria, S. Berneschi, M. Brenci, F. Cosi, G. Nunzi Conti, S. Pelli, G. C. Righini, Optical microspherical resonators for biomedical sensing, *Sensors* 11 (1) (2011) 785–805.
- [35] E. Nuhiji, P. Mulvaney, Detection of unlabeled oligonucleotide targets using whispering gallery modes in single, fluorescent microspheres, *Small* 3 (8) (2007) 1408–1414.
- [36] J. A. Stratton, *Electromagnetic theory*, International series in pure and applied physics, McGraw-Hill, New York, NY, 1941.
- URL <https://cds.cern.ch/record/105763>
- [37] E. Hill, The theory of vector spherical harmonics, *American Journal of Physics* 22 (4) (1954) 211–214.
- [38] B. Johnson, Theory of morphology-dependent resonances: shape resonances and width formulas, *JOSA A* 10 (2) (1993) 343–352.
- [39] F. Treussart, *Etude expérimentale de l’effet laser dans des microsphères de silice dopées avec des ions neodyme*, Theses, Université Pierre et Marie Curie - Paris VI (Dec. 1997).
- URL <https://tel.archives-ouvertes.fr/tel-00011781>
- [40] J.-B. Ceppe, *Eléments de dynamique du laser pour l’élaboration d’une source micro-onde miniaturisée sur la base de la double émission monomode d’un laser à mode de galerie*, Ph.D. thesis, Université Rennes 1 (2018).
- URL <http://www.theses.fr/2018REN1S067>
- [41] Eshelby John Douglas, Peierls Rudolf Ernst, The elastic field outside an ellipsoidal inclusion, *Proceedings of the Royal Society of London. Series A. Mathematical and Physical Sciences* 252 (1271) (1959) 561–569. doi:10.1098/rspa.1959.0173.
- URL <https://royalsocietypublishing.org/doi/10.1098/rspa.1959.0173>

- [42] P. Bechterew, Analytical study of the generalized Hooke's law. Application of the method of coordinate transformation, *Zh. Russ. Fiz.-Khim. Obshch.* 58 (1926) 415–446.
- [43] R. Gafsi, M. A. El-Sherif, Analysis of induced-birefringence effects on fiber bragg gratings, *Optical Fiber Technology* 6 (3) (2000) 299–323.
- 365 [44] M. L. M. François, C. Guigot, Y. Lecieux, C. Lupi, D. Leduc, Dispositif tridimensionnel de mesure des déformations locales (Patent application FR2013104).
- [45] M. L. M. François, Y. Lecieux, A 6-ring embedded strain sensor, Submitted to *Meccanica*.
- [46] W. Primak, D. Post, Photoelastic constants of vitreous silica and its elastic coefficient of refractive index, *Journal of Applied Physics* 30 (5) (1959) 779–788.
- 370 [47] A. Bertholds, R. Dandliker, Determination of the individual strain-optic coefficients in single-mode optical fibres, *Journal of lightwave technology* 6 (1) (1988) 17–20.
- [48] L. Durvasula, R. W. Gammon, Brillouin scattering from shear waves in amorphous polycarbonate, *Journal of Applied Physics* 50 (6) (1979) 4339–4344.
- 375 [49] G. Ramachandran, Photoelastic constants of diamond, in: *Proceedings of the Indian Academy of Sciences-Section A*, Vol. 25, Springer, 1947, p. 208.
- [50] P. Djemia, K. Bouamama, Ab-initio calculations of the photoelastic constants of the cubic polytype, in: *Journal of Physics: Conference Series*, Vol. 454, IOP Publishing, 2013, p. 012060.
- 380 [51] E. Jog, R. Krishnan, Dispersion of the photoelastic constants of fused silica, *Nature* 179 (4558) (1957) 540–541.
- [52] D. K. Biegelsen, J. C. Zesch, Optical frequency dependence of the photoelastic coefficients of fused silica, *Journal of Applied Physics* 47 (9) (1976) 4024–4025.
- [53] Y.-Z. Yan, C.-L. Zou, S.-B. Yan, F.-W. Sun, Z. Ji, J. Liu, Y.-G. Zhang, L. Wang, C.-Y. Xue, W.-D. Zhang, et al., Packaged silica microsphere-taper coupling system for robust thermal sensing application, *Optics express* 19 (7) (2011) 5753–5759.
- 385 [54] J. Botsis, L. Humbert, F. Colpo, P. Giaccari, Embedded fiber bragg grating sensor for internal strain measurements in polymeric materials, *Optics and lasers in Engineering* 43 (3-5) (2005) 491–510.

- 390 [55] A. Shukla, B. Agarwal, B. Bhushan, Determination of stress intensity factor in orthotropic composite materials using strain gages, *Engineering fracture mechanics* 32 (3) (1989) 469–477.
- [56] S. Budhe, M. Banea, S. De Barros, L. Da Silva, An updated review of adhesively bonded joints in composite materials, *International Journal of Adhesion and Adhesives* 72 (2017) 30–42.
- 395 [57] M. Girard, M. Péron, A. Uguen, P. Casari, F. Jacquemin, A simple characterization methodology for the identification of the visco-elastic behavior of thermoset adhesives during cure, *Applied Adhesion Science* 8 (1) (2020) 1–14.